Nanoscale

PAPER

View Article Online
View Journal | View Issue

Check for updates

Cite this: *Nanoscale*, 2025, **17**, 21535

Chemically deposited Cu nanocubes on a PUA gyroid lattice for lightweight and flexible electromagnetic interference shielding

Yingying Ma,[a] Udeshwari Jamwal,[b] Shixiang Zhou,[a] Zhicheng Wei,[a] Wentao Yan,[c] Yong Yang *[b] and Jun Ding *[a]

Electromagnetic pollution poses significant risks to electronic devices and human health, highlighting the need for mechanically robust, lightweight, and cost-effective electromagnetic interference (EMI) shielding materials. 3D-printed structures with nanomaterial-engineered surfaces offer a promising method for tailoring mechanical and electrical properties through multiscale design. Herein, we present a facile strategy for fabricating lightweight and flexible EMI shielding structures by chemical deposition of nanostructured metal coatings onto 3D-printed polymeric substrates. Copper nanocube-decorated polyurethane acrylate (Cu/PUA) structures with triply periodic minimal surface (TPMS) architectures are fabricated to materialize this design. The densely arrayed nanocubes enhance electrical conductivity and enlarge the interfacial surface area, while the continuous curvature and interconnected porosity of the TPMS design promote multi-reflection and internal absorption of incident electromagnetic waves. Thus, gyroid-structured Cu/PUA achieves an average total shielding effectiveness of 76.64 dB in the X band, corresponding to an attenuation of 99.999998% of incident waves. Despite an ultralow density (0.41 g cm^{-3}), the material exhibits an excellent compressive strength of 0.54 MPa and a flexural strength of 0.51 MPa. This approach offers a scalable and versatile route to multiscale synergistic modification, demonstrating the potential of architected nanostructured composites for EMI shielding applications.

Received 30th May 2025,
Accepted 20th August 2025

DOI: 10.1039/d5nr02300a

rsc.li/nanoscale

Introduction

Electromagnetic interference (EMI) shielding materials play an indispensable role in modern society, as wireless communication systems increasingly generate electromagnetic pollution that poses potential risks to electronic instruments and human health.[1,2] This is particularly critical for aerospace components, precision industrial equipment, and wearable electronics, where EMI shielding materials must provide both electromagnetic protection and mechanical integrity.[3,4] Furthermore, lightweight designs are highly desirable to minimize additional structural load, thereby extending the operational lifespan of such systems.[5] Metals are widely employed as EMI shielding materials due to their high electrical conductivity, which induces a strong impedance mismatch.[6] Polymeric materials offer advantages in light weight and processability but lack sufficient electrical conductivity to achieve effective EMI shielding performance. However, achieving sufficient shielding effectiveness typically requires metallic shields to possess considerable thickness, which significantly compromises weight and cost efficiency. When metals are processed into mesh-like structures to reduce weight, their mechanical durability is often diminished. Therefore, the development of a general strategy to fabricate EMI shielding components that simultaneously offer high conductivity, low density, and mechanical robustness is of great significance for enabling dual electromagnetic and structural protection.[7]

Polymer matrix composites integrate the advantageous properties of polymers with those of functional modifiers, offering a combination of light weight, flexibility, and cost-effectiveness,[4,8] making them highly promising candidates for EMI shielding applications.[9,10] Notably, the formability of polymeric materials makes them well-suited for various 3D printing technologies, enabling the realization of structure-induced functionalities that are challenging to achieve using conventional bulk materials. Triply periodic minimal surface (TPMS) geometries, defined by their periodicity and zero mean curvature, exhibit a unique combination of low density and high mechanical strength,[11,12] often surpassing traditional

---

[a] *Department of Materials Science and Engineering, National University of Singapore, 9 Engineering Drive 1, 117575, Singapore. E-mail: msedingj@nus.edu.sg*

[b] *National University of Singapore, 5A Engineering Drive 1, 117411, Singapore. E-mail: tslyayo@nus.edu.sg*

[c] *Department of Mechanical Engineering, National University of Singapore, 9 Engineering Drive 1, 117575, Singapore*

lattice structures in terms of specific strength (strength-to-density ratio).[13,14] Additionally, the inherent geometric uniformity of TPMS structures facilitates isotropic load distribution, thereby overcoming the direction-dependent mechanical limitations associated with honeycomb-like architectures.[15,16] Through tunable parameters such as pore size and specific surface area, TPMS-based designs allow for the integrated optimization of structure, function, and performance. Polyurethane acrylate (PUA) is a highly suitable candidate for 3D printing of TPMS structures due to its UV-curable nature, enabling high-resolution fabrication *via* vat photopolymerization techniques.[17,18] PUA contains both acrylic functional groups and amino ester bonds, which, upon curing impart a synergistic combination of wear resistance, flexibility, low-temperature tolerance typical of polyurethanes, and the superior weatherability associated with polyacrylates. As a result, 3D-printed PUA structures can accurately materialize complex TPMS geometries while harnessing their mechanical and structural advantages.

The incorporation of nanomaterials onto TPMS-structured PUA substrates enables the realization of functional architectures with tailored properties across multiple length scales from the macro to nanoscale.[19,20] Chemical deposition, also known as electroless plating, offers distinct advantages for the functionalization of complex 3D-printed geometries. This solution-based process relies on redox reactions, in which a reducing agent facilitates the spontaneous reduction of metal ions into metallic atoms that conformally deposit onto the substrate surface. Thus, chemical deposition allows for uniform metal coating over intricate architectures, including internal channels, deep pores, and high-aspect-ratio features. Key process parameters such as temperature, pH, and solution composition can be finely tuned to modulate the deposition rate and film morphology. The resulting metallic coatings typically exhibit high uniformity, strong interfacial adhesion, and tunable composition. As a highly conductive and cost-effective metal, copper is particularly well-suited for the electroless modification of TPMS-structured PUA for EMI shielding applications. Through *in situ* reduction, Cu can nucleate homogeneously on the polymeric surface and grow into dense nanostructured coatings.[8] These nanostructures significantly improve the electrical conductivity of the PUA, while the increased interfacial area promotes enhanced impedance mismatch at the air–material interface. Furthermore, the intrinsic porosity and interconnected architecture of TPMS geometries facilitate multiple internal reflections of incident electromagnetic waves, thereby enhancing reflection loss and further improving shielding effectiveness.[10] Importantly, these enhancements in functional performance are achieved without compromising the lightweight and mechanically robust nature of the PUA substrate.

Consequently, we present a general strategy for the fabrication of lightweight, flexible, and highly porous EMI shielding structures by chemically depositing nanostructured metal coatings onto 3D-printed polymer lattice substrates (PLS). To materialize this design, Cu nanocube-decorated PUA structures with TPMS architectures, including gyroid, diamond, and I-WP geometries, were fabricated *via* digital light processing (DLP). The Cu nanocubes were conformally deposited onto the TPMS structures through an *in situ* chemical reduction process, resulting in a substantial increase in electrical conductivity from insulation to 57 904.7 S m^{-1}. The nanocube morphology not only enhances electrical performance but also increases the interfacial surface area, thereby improving electromagnetic wave scattering. Among the geometries, the gyroid-structured Cu/PUA composite exhibited the highest average total shielding effectiveness of 38.29 dB in the X-band with 2 mm thickness. The uniform decoration of Cu nanocubes also contributes to broadband and consistent shielding performance. Further improvement in EMI shielding was observed with increased structural thickness, where a 6 mm-thick gyroid sample achieved an average shielding effectiveness of 76.64 dB, attributed to its continuous curvature and interconnected pore network that facilitates multireflection pathways. The Cu/PUA gyroid structure maintained a low density of 0.41 g cm^{-3}, alongside high mechanical robustness, exhibiting compressive and flexural strengths of 0.54 MPa and 0.51 MPa, respectively. These results demonstrate a multiscale-engineered EMI shielding structure that effectively integrates structural, electrical, and mechanical functionalities.

Results and discussion

Configuration design of Cu/PUA TPMS structures for EMI shielding

The fabrication of Cu-coated PLSs started with a Digital Light Printing (DLP) process, and diamond, gyroid, and I-wrap solid networks were constructed. Then the PLSs were coated with Cu by the chemical deposition method (Fig. 1a). The successful coating of Cu on the PLS surface was verified by a change in the apparent color (Fig. 1c) from grey to brick red. The bonding strength of the Cu coating layer was tested to be 3B according to ASTM D3359-23, indicating relatively good adhesion (Fig. S1, SI). As depicted in Fig. 1b, the XRD spectrum of the PUA substrate exhibited irregular peaks in the whole scan range due to its amorphous structure. After Cu coating, Cu/PUA showed distinct peaks at 44.0°, 51.1° and 74.8°, corresponding to the (111), (200) and (220) lattice planes of Cu.[21,22] A positive shift of Cu diffraction peaks (~0.7°) was observed compared with standard PDF#04-0836. The Cu/PUA material showed a substantial enhancement in conductivity (57 904.70 S m^{-1}) compared with the original PUA material (0.00 S m^{-1}).

Notably, as shown in Fig. 1d, the Cu-coating method has proven to be effective for other kinds of materials, such as polylactic acid (PLA) and silicon oxycarbide (SiOC) in our study, demonstrating excellent adaptability across various materials. The conformal deposition capability renders this method well-suited for a wide range of intricate geometries, ensuring high coating uniformity throughout complex structures.

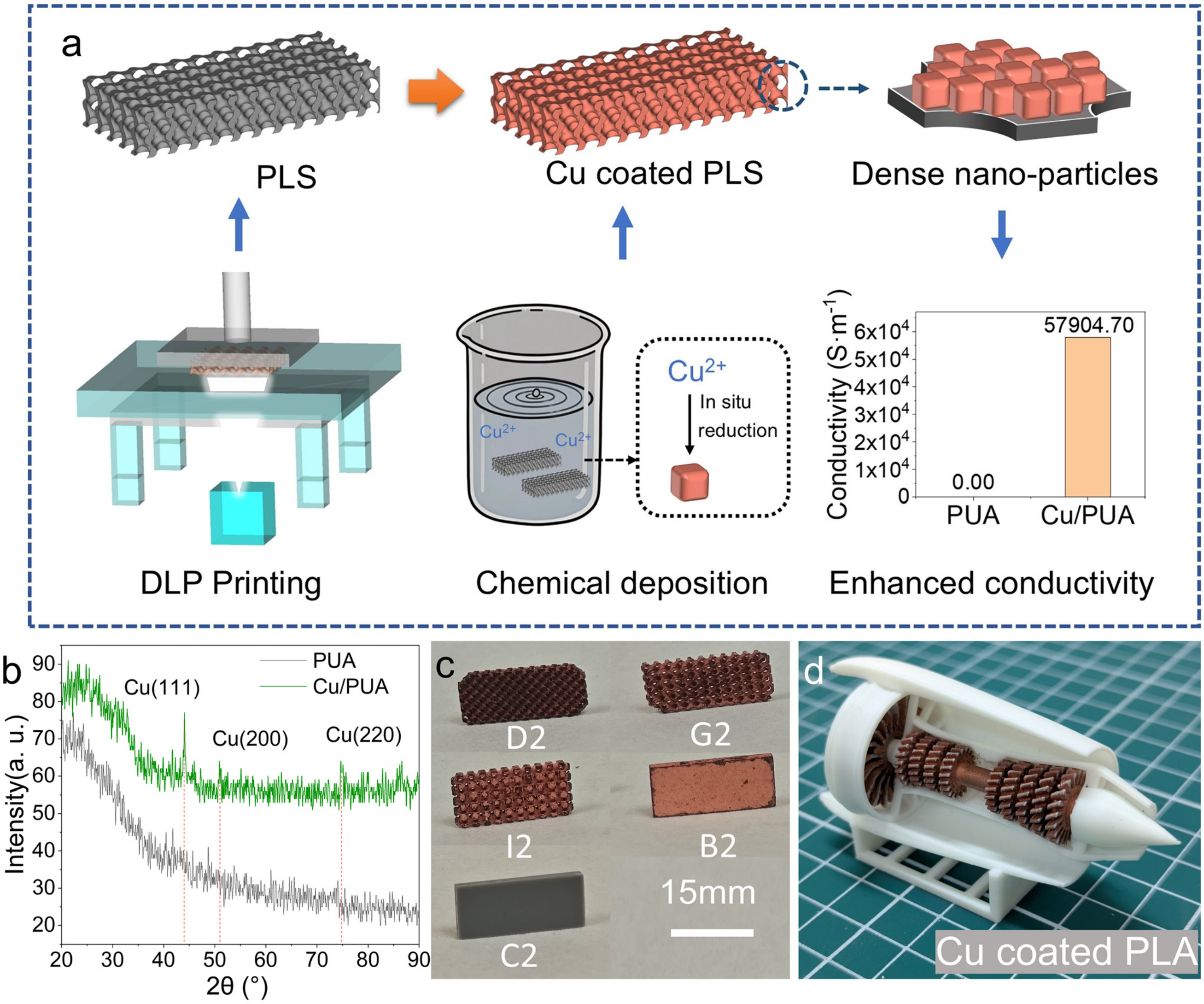

Fig. 1 (a) Schematic illustrations of the fabrication process of Cu coated PUA TPMS structures. (b) The XRD patterns of PUA and Cu/PUA samples. (c) The fabricated samples with 2 mm thickness. (d) Cu coated polylactic acid (PLA) model.

Electromagnetic interference (EMI) shielding performance and surface morphology of Cu/PUA PLSs

The EMI shielding effectiveness of all samples with 2 mm thickness (C2, B2, D2, G2, I2), including total shielding effectiveness (SE_T), as well as the contribution of reflection (SE_R) and absorption (SE_A) at a frequency of 8.2–12.4 GHz, is shown in Fig. 2b–f. Fig. 2b shows that the SE_T value of the C2 sample remained stable in a range of 1.86–2.14 dB within the whole frequency range, indicating a poor shielding performance of the PUA bulk material. After being coated with Cu, the SE_T value of B2 (Fig. 2c) increased dramatically to 18.10–20.39 dB. Compared with B2, the SE_T of D2, G2 and I2 improved further with dual increments in SE_A and SE_T, demonstrating the effectiveness of the TPMS structure for enhancing EMI shielding performance. Specifically, the D2 sample (Fig. 2d) showed relatively consistent SE_T values (34.16–37.73 dB) across the whole frequency range. In contrast, the SE_T value of the G2 sample (Fig. 2e) exhibits a unimodal distribution ranging from 30.29 to 42.71 dB, with a higher SE_T value for a high frequency range (10–12 GHz). For the G2 sample, the maximum SE_T value reached 42.71 dB at a frequency of 10.97 GHz. The SE_T values of the I2 sample in Fig. 2f showed a bimodal distribution within the range of 21.71–27.52 dB. In general, D2 and G2 samples exhibited better SE_T and G2 showed a higher peak SE_T value.

The morphology of the original PUA and Cu/PUA surface was observed by SEM and the results are shown in Fig. 2g and h. As displayed in Fig. 2g, the surface of un-coated PUA was generally smooth, with some randomly distributed particles. After Cu-coating, the PUA surface was evenly covered with a thin layer of scaly Cu (Fig. 2h). Higher magnification (200 kx) was applied to observe the microstructures on the scales, as shown in Fig. 2i, the surface of the scales is covered with

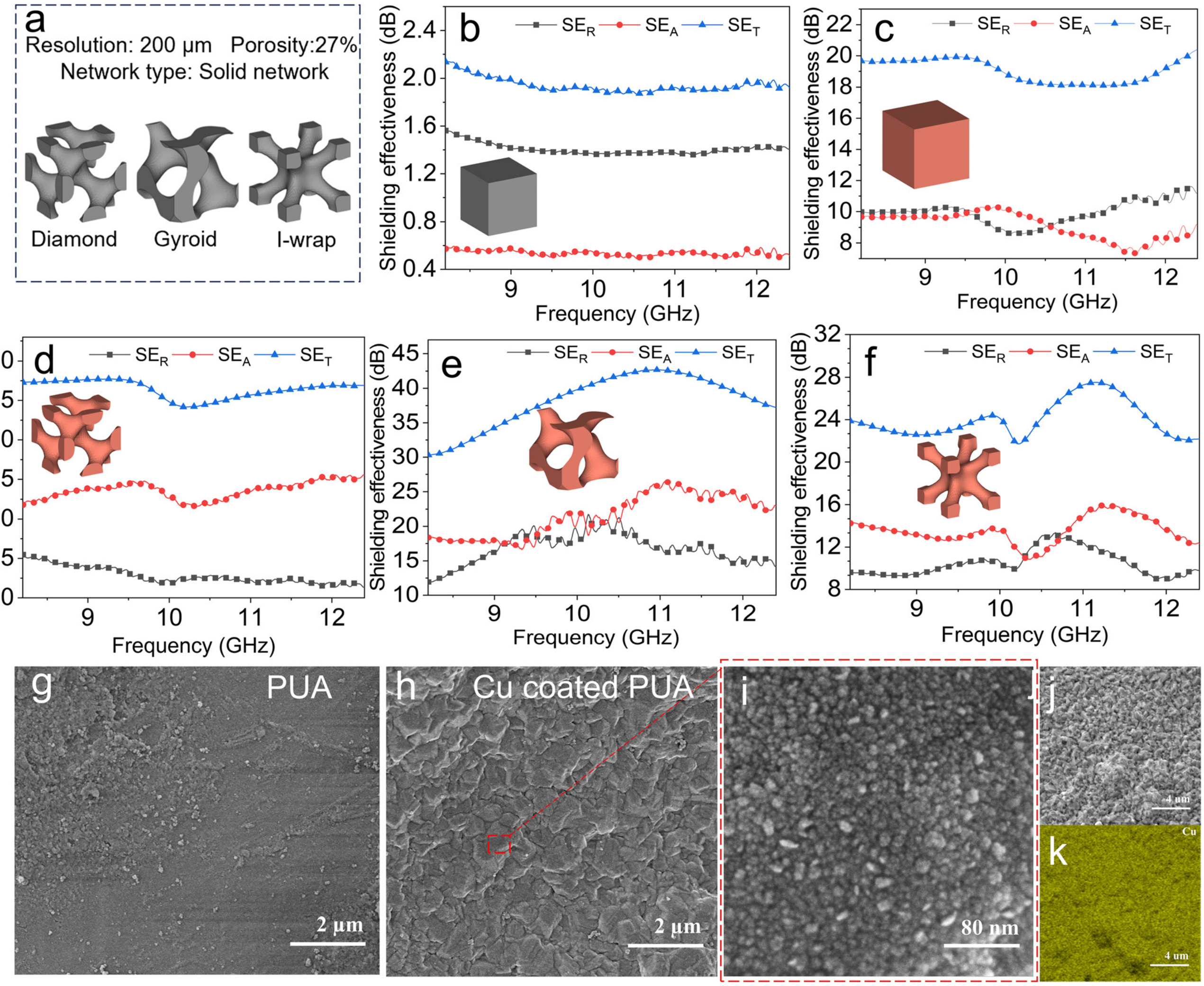

Fig. 2 (a) The cell structure and design parameters of diamond, gyroid and I-wrap structures. (b) The SE$_R$, SE$_A$ and SE$_T$ of the C2 sample (without Cu coating). (c) The SE$_R$, SE$_A$ and SE$_T$ of the B2 sample (with Cu coating). (d) The SE$_R$, SE$_A$ and SE$_T$ of the D2 sample. (e) The SE$_R$, SE$_A$ and SE$_T$ of the G2 sample. (f) The SE$_R$, SE$_A$ and SE$_T$ of the I2 sample. (g) The surface of the original PUA material at 10KX magnification. (h) The surface of the Cu-coated PUA material at 10KX magnification. (i) The surface of the Cu-coated PUA material at 200KX magnification. (j) The region on Cu-coated PUA for EDS mapping. (k) The EDS mapping of Cu elements.

dense spherical Cu nanocubes. The highly interconnected TPMS structures with dense Cu nanocubes enhanced the inner reflection and scattering and led to better EM wave reflection and absorption. Fig. 2j and k show the original regions for EDS mapping and the distribution of Cu elements, which further verified the successful coating of Cu on the sample surface.

Surface composition and shielding mechanism of gyroid-structured Cu/PUA PLSs

The elemental composition and chemical states of the Cu-coated sample were characterized by XPS. As shown in Fig. 3a, the sample was composed of Cu, O and C elements, which corresponded to the EDS mapping results (Fig. 3c). Fig. 3b shows the Cu 2p fraction spectra of the Cu-coated material. Peaks in the range of 925–944 eV belonged to Cu 2p$_{3/2}$ orbitals and peaks in the range of 944–965 eV belonged to Cu 2p$_{1/2}$ orbitals.[23,24] The peaks at 927.90 eV and 947.76 eV belonged to Cu^0 and the peaks at 930.10 eV and 950.01 eV belonged to Cu^{2+}.[22] The presence of Cu^{2+} was attributed to partial oxidation of the coating layer by oxygen in air.

Fig. 3d illustrates the average SE$_T$, SE$_R$ and SE$_A$ for all the samples with 2 mm thickness. All TPMS structures showed higher SE$_R$ and SE$_A$ compared to control groups C2 and B2, indicating the effectiveness of TPMS structures in promoting EMI reflection and absorption for Cu-coated PUA. For the optimal G2 sample, the SE$_T$ value was 27.16 times that of C2 and 2.01 times that of B2. Among the three kinds of PLSs, G2 had the highest average SE$_T$ value of 38.29 dB, which means that 99.99% of the incident EM waves were shielded. The reasons that the G2 sample showed the highest average SE$_T$ value among all TPMS structures can be summarized in

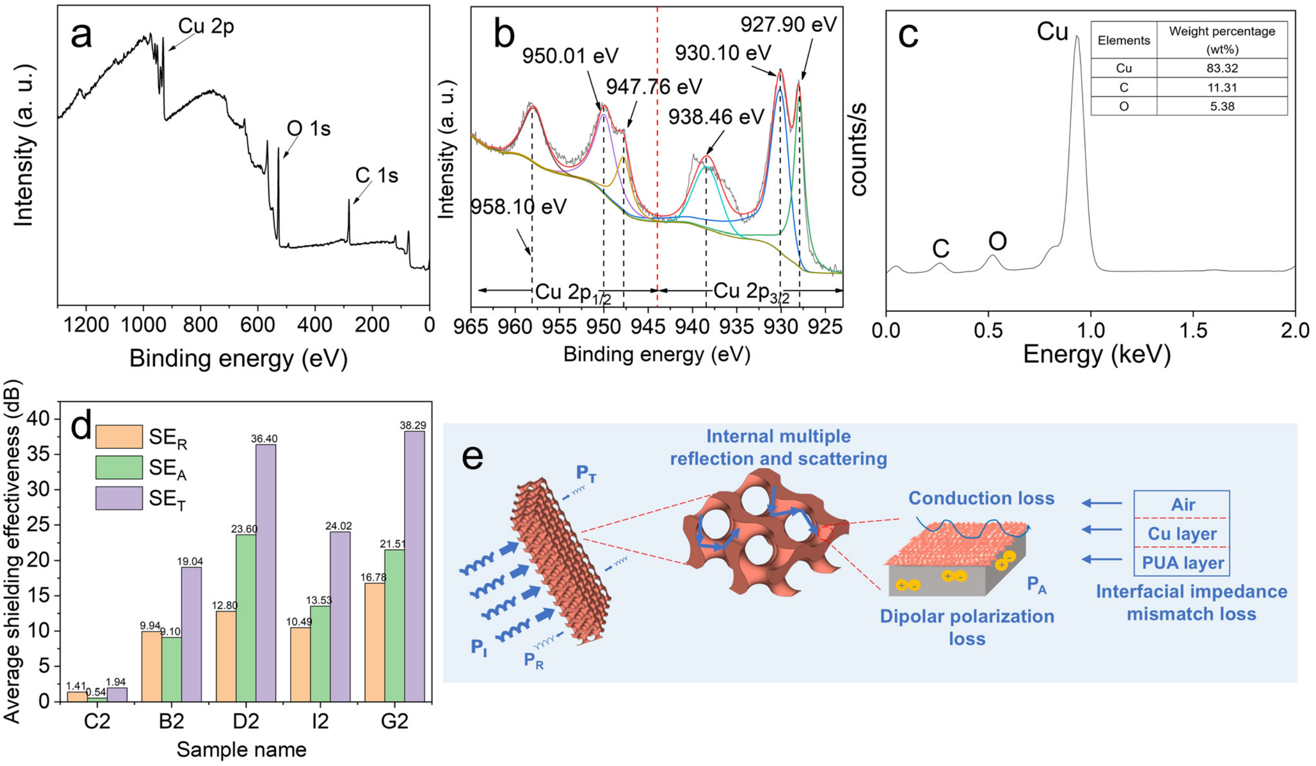

Elements	Weight percentage (wt%)
Cu	83.32
C	11.31
O	5.38

Fig. 3 (a) The XPS survey scan of the Cu-coated PUA material. (b) The Cu 2p fraction spectra of the Cu-coated PUA material. (c) The EDS spectrum of the Cu-coated PUA material. (d) The average EMI shielding effectiveness of samples of 2 mm thickness in a frequency range of 8.2–12.4 GHz. (e) The EMI shielding mechanism of the Cu-coated gyroid structure.

two aspects. Firstly, the G2 sample showed the highest average SE_R compared with D2 and I2, which was attributed to its intensified reflection induced by internal helical channels with continuous curvature.[25] Secondly, as shown in Fig. 2e, the G2 sample had a higher SE_A value towards high frequency EM waves, with a peak value appearing at 11.07 GHz. Specifically, the cell structure of the G2 sample enabled the formation of a helical resonant cavity, within which electromagnetic waves of certain frequencies were strongly dissipated.[26] Other studies also indicated that the gyroid structure had an ultrawide absorption bandwidth[27] and superior EMI shielding performance within the THz range.[7]

Fig. 3e shows the shielding mechanism of gyroid-structured Cu/PLSs. When incident EM waves reach the surface of Cu/PUA, part of the EM waves was reflected. The penetrated waves will be trapped by the continuous gyroid structure and dissipated by the multiple internal reflections and scattering.[28] During the reflection and scattering process, the EM waves could be diminished by propagation loss and material loss. (1) For propagation loss, the multiple internal reflection and scattering extend the propagation path of EM waves and lead to energy attenuation. The highly-porous structure of TPMS substrates and Cu scales covered with Cu nanocubes can provide an abundant surface for second reflection. Besides, the destructive interference between the original and reflected waves can also reduce the energy of EM waves. (2) For material loss, the EM waves can be effectively consumed through three mechanisms: conduction loss, interfacial impedance mismatch loss and dipolar polarization loss. There is an induced current in the highly-conductive surface Cu layer under EM radiation and the energy is consumed by the Ohmic effect, which is the main contributor to conduction loss. The huge conductivity difference between air, the Cu layer, and the PUA substrate forms a sandwich-structured conjunction, leading to substantial interfacial impedance mismatch loss. Finally, when EM waves penetrate into the PUA substrate, the dipolar polarization loss caused by polarization hysteresis of dipoles will lead to further consumption of energy of EM waves. In general, it is the enhanced reflection, propagation loss and material loss of the Cu/PUA gyroid structure that led to superior EMI shielding performance.

The influence of thickness, TPMS structure and Cu coating on EMI shielding performance

The influence of some key factors, including thickness, TPMS structure and Cu coating, on EMI shielding effectiveness was investigated through control experiments. As depicted in Fig. 4a, gyroid-structured Cu/PLSs, Cu/PUA bulk samples, gyroid-structured PLSs and PUA bulk samples with different thicknesses (2 mm, 4 mm, and 6 mm) were fabricated and named G-series, B-series, GL-series and C-series, respectively.

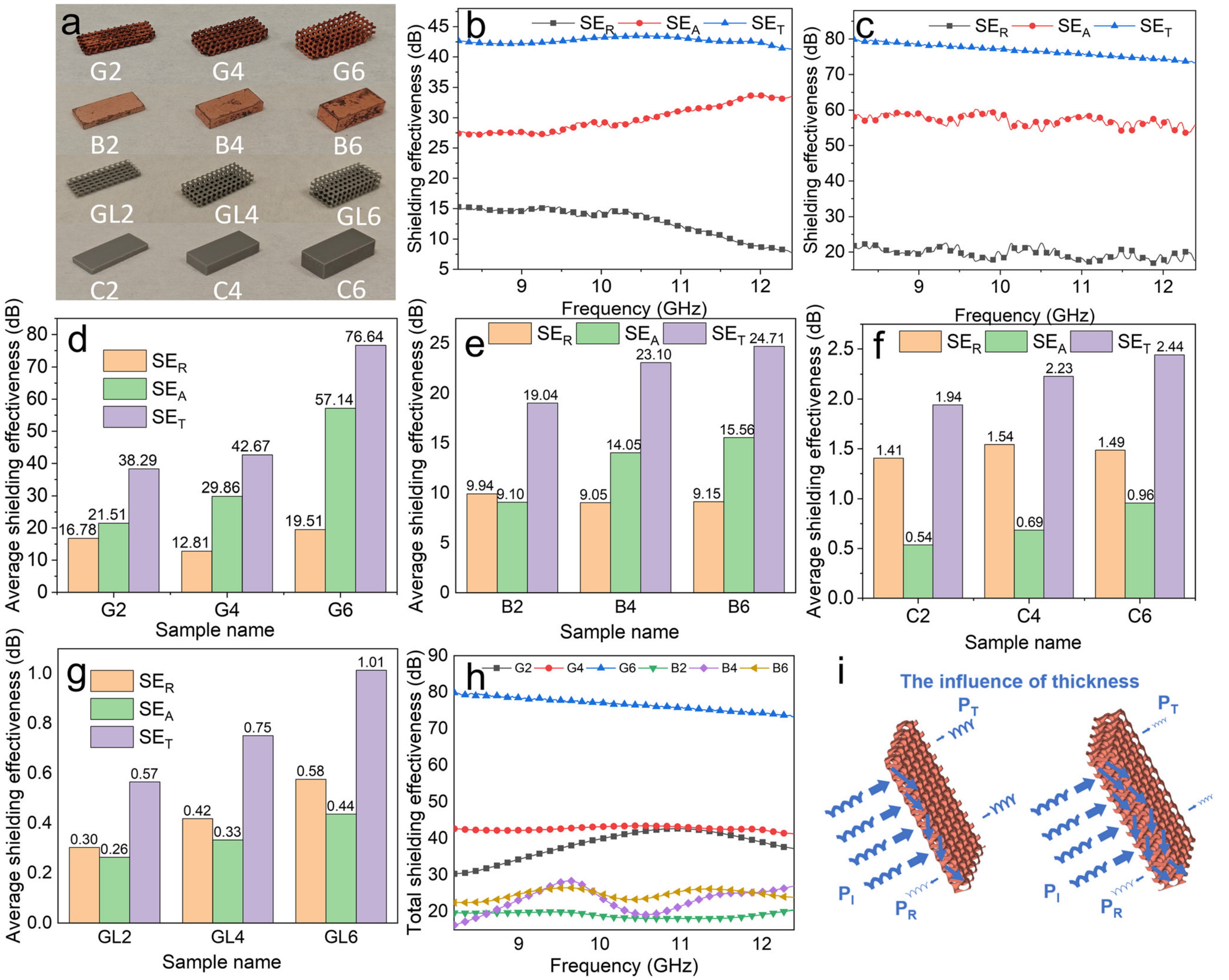

Fig. 4 (a) The fabricated samples of different thicknesses for the EMI shielding test: gyroid-structured samples with Cu coating (G2, G4, and G6), bulk samples with Cu coating (B2, B4, and B6), gyroid-structured samples without Cu coating (GL2, GL4, and GL6) and bulk samples without Cu coating. (b) The SE_R, SE_A, and SE_T of the G4 sample. (c) The SE_R, SE_A, and SE_T of the G6 sample. (d) The average EMI shielding effectiveness of G2, G4, and G6 samples in a frequency range of 8.2–12.4 GHz. (e) The average EMI shielding effectiveness of B2, B4, and B6 samples in a frequency range of 8.2–12.4 GHz. (f) The total EMI shielding effectiveness of C2, C4, and C6 samples in a frequency range of 8.2–12.4 GHz. (g) The average EMI shielding effectiveness of GL2, GL4, and GL6 samples in a frequency range of 8.2–12.4 GHz. (h) The total EMI shielding effectiveness of G-series and B-series samples in a frequency range of 8.2–12.4 GHz. (i) The influence of thickness.

As shown in Fig. 4b and c, The SE_T values of G4 and G6 increased with thickness. For the G4 sample, the SE_T was in a range of 41.27–43.48 dB. For the G6 sample, the SE_T was in a range of 72.70–81.26 dB, showing superior total shielding effectiveness for all tested frequencies.

Fig. 4d–g showed the average SE_R, SE_A, and SE_T values of the samples displayed in Fig. 4a. From Fig. 4d, the average SE_T values for G2, G4 and G6 were 38.29 dB, 42.67 dB, and 76.64 dB, respectively. For the G6 sample, the SE_T was 3.10 times that of B6 and 99.999998% of the incident EM waves were shielded. To verify the reliability of the test result, a parallel G6 sample (G6-P) was fabricated and a replicate experiment was conducted for its EMI shielding effectiveness (Fig. S2). The average SE_T value for parallel G6-P was 74.73 dB, with an acceptable relative error of 2.49%. Except for the G-series, the average SE_T and SE_A values also witnessed a gradual increase with thickness across all other sample series, which was mainly attributed to the long propagation path. As shown in Fig. 4h, SE_T increased with thickness for both Cu/PLSs and Cu/PUA bulk samples, but the increment of SE_T with thickness was dramatically higher for Cu/PLSs compared with Cu/PUA bulk samples.

The comparison between G-series/GL-series (Fig. 4d and g) and B-series/C-series (Fig. 4e and f) illustrated the influence of Cu coating. Cu coating led to a significant increase in both SE_R and SE_A values for G-series and B-series, indicating strengthened EMI reflection and absorption, which might be caused by the interfacial impedance mismatch induced by the distinct impedance difference between air/Cu/polymer interface.[29]

The effects of the gyroid structure on EMI shielding could be concluded by comparing the shielding effectiveness of G-series/B-series (Fig. 4d and e) and GL-series/C-series (Fig. 4g and f). Notably, the introduction of the gyroid structure had contrary effects for samples with and without Cu coating, manifesting as increased SE_R and SE_A in Cu-coated samples and decreased SE_R and SE_A in uncoated samples. This was caused by the inherent characteristics of highly interconnected helical channels of the gyroid structure. For uncoated samples, the porous structure led to a multiplied possibility for direct penetration of EM waves, resulting in a decline in SE_T. However, for Cu-coated samples, the adverse effects of EM wave penetration were surpassed by energy attenuation resulting from a prolonged helical propagation path, strengthened reflection induced by an enlarged reflection area as well as enhanced absorption due to augmented material loss. The EMI shielding performance of diamond and I-wrap-structured PLSs without Cu-coating (DL2, GL2) could be found in the SI (Fig. S3), and they both showed decreased SE_T compared with C2, similar to that of GL2.

Fig. 4i presented a comprehensive illustration of the influence of all factors; it was the cumulative effects of augmented thickness, impedance mismatch induced by Cu-coating and highly interconnected channels of the gyroid structure that led to the superior EMI shielding performance of the G6 sample.

A comprehensive comparison with other previously-reported EMI shielding materials is presented in Table 1. Most EMI shielding materials reported lack mechanical strength evaluation. MXenes were common components among EMI shielding materials; although they exhibited ultra-low density (0.0109 g cm^{-3}) with relatively high EMI shielding performance (26–33 dB), the lack of mechanical strength undermined their potential for practical application.[30] $Ti_3C_2T_x$-PVA showed satisfactory EMI shielding performance but it was also hindered by a low compressive strength of 0.215 MPa.[31] In this work, Cu/PUA PLSs showed satisfactory and balanced performance in terms of EMI shielding effectiveness, density and mechanical strength, which enhances their attractiveness for industrial applications. Besides, this study also provides a versatile method for Cu chemical coating and effective construction of an EMI shielding system, applicable to the development of diverse functional materials.

Mechanical properties

A material compression test was conducted according to the ASTM D1621 standard and the results are shown in Fig. 5a. The compression behavior of diamond, gyroid and I-wrap samples consisted of three stages: the linear elastic stage, the plastic plateau stage and the densification stage. The compressive strength of the samples was defined as the stress at 10% deformation. Apparently, the gyroid structure showed the highest compressive strength (0.54 MPa). Besides, there was no obvious yield point for diamond and the gyroid structure during the whole compression test, suggesting a progressive deformation. For the I-wrap structure, the yield point occurred at 60.96% strain and the obvious structure fracture was observed simultaneously.

A three-point bending test was conducted according to the ASTM D790 standard and the results are displayed in Fig. 5b. As shown in Fig. 5b, the gyroid structure showed the highest flexural stress of 0.51 MPa at 1.19% flexural strain.

The cyclic loading behavior of the materials was also investigated and the results are displayed in Fig. S4 (SI). Both cyclic compressive and cyclic flexural processes revealed a gradually stabilized softening effect, as indicated by the substantial difference between cycle 1 and cycle 8 and a negligible difference between cycle 8 and cycle 20. Residual strain and stress were observed due to the presence of plastic deformation under cyclic loading. The material remained in good condition after 20 cycles, indicating high durability.

COMSOL simulation was used to evaluate the impact resistance of different structures (Fig. 5d). The impact resistance was evaluated by von Mises stress distribution at the maximum contact force. For diamond, gyroid and I-wrap structures, the maximum contact force occurred at 0.0003 s, 0.0005 s, and

Table 1 The comparison of EMI shielding performance and mechanical properties between this work and other literature reports

Materials	Thickness (mm)	Frequency (GHz)	Density (g cm^{-3})	SE_T (dB)	Compressive strength (MPa)	Flexural strength (MPa)	Ref.
MXene/PVA	5	8.2–12.4	0.0109	26–33	—	—	30
$Ti_3C_2T_x$ MXene/Epoxy	2	8.2–12.4	—	41	—	—	31
PI	2.5	8.2–12.4	0.085–0.125	26.1–28.8	0.33	—	32
CNT/EP	3	8.2–12.4	—	53.14	400	—	33
Ti_3C_2 MXenes	1	8.2–12.4	—	32	—	—	34
$NiFe_2O_4$/graphene	2	8.2–12.4	—	31–34	—	—	35
PU/MXene	3	8.2–12.4	—	56.86	—	—	36
PI/PANI-GO	2	8.2–12.4	0.56	28.2	—	—	37
GNs-CNTs/CMF	3	8.2–12.4	0.03	35.4	—	—	38
Graphene network/PU	2	8.2–12.4	—	35.6	—	—	39
PVDF-based foams	1	8.2–12.4	—	32.2	—	—	40
Needle-like Co_3O_4/C array	1.63	8.2–12.4	—	33	—	—	41
$Ti_3C_2T_x$-PVA	5	8.2–12.4	0.1	70	0.215	—	10
Cu/PUA	6	8.2–12.4		72.7	0.54	0.51	This work
Cu/PUA	2	8.2–12.4		38.29	0.54	0.51	This work

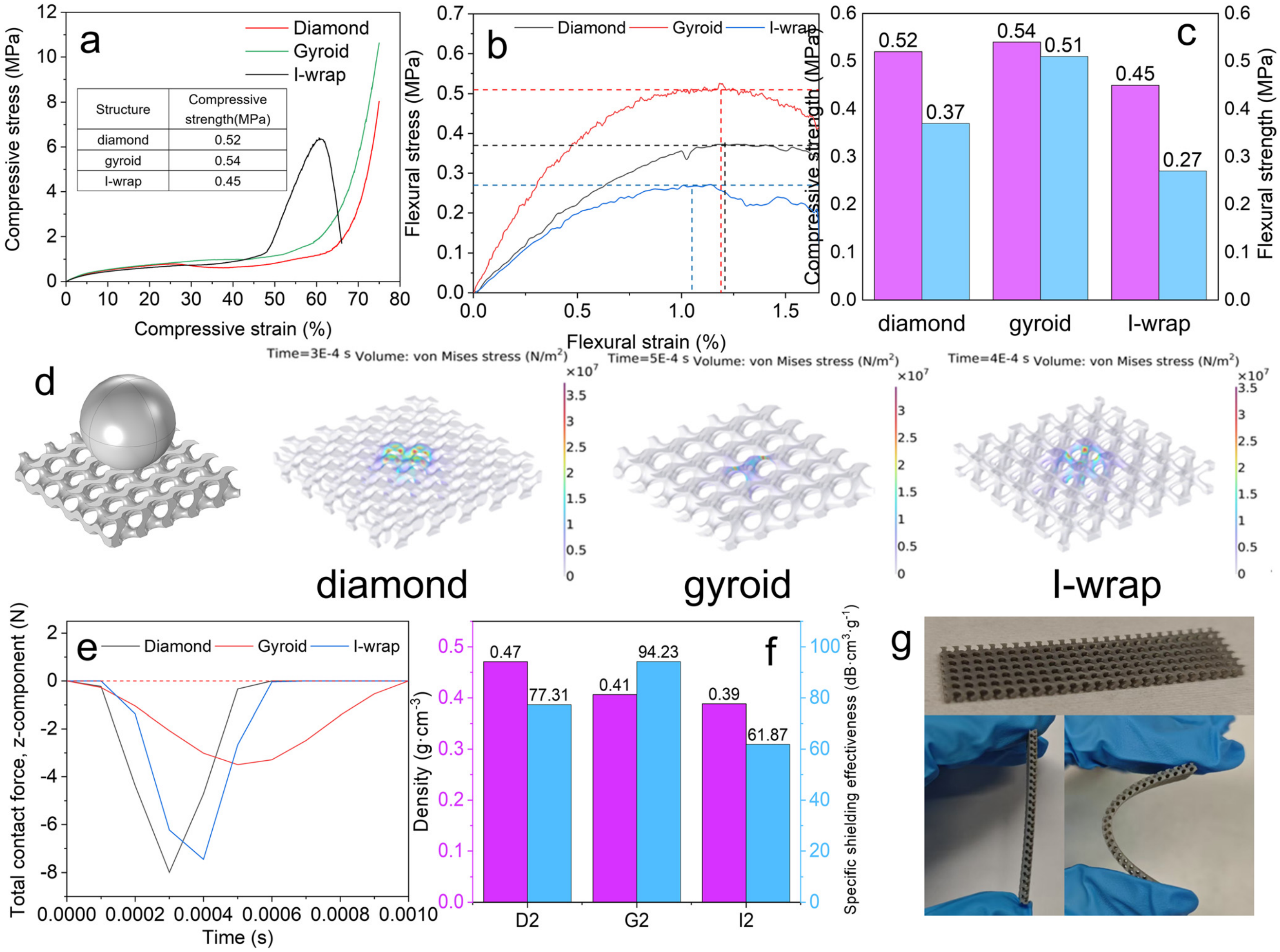

Fig. 5 (a) The compressive strain–stress curves of diamond, gyroid and I-wrap samples. (b) The flexural strain–stress curves of diamond, gyroid and I-wrap samples. (c) The compressive strength and flexural strength of diamond, gyroid and I-wrap samples. (d) The model setup and von Mises stress distribution of diamond, gyroid, and I-wrap structures at maximum contact force by COMSOL simulation. (e) The contact force curves of diamond, gyroid and I-wrap structures by COMSOL simulation. (f) The density and specific shielding effectiveness of D2, G2, and I2 samples. (g) The superior flexibility of Cu/PLSs.

0.0004 s, respectively (Fig. 5e). The contact force curve of gyroid showed a more gradual slope compared with that of diamond and I-wrap. Fig. 5d indicates that the maximum volume von Mises stress for diamond, gyroid and I-wrap structures was 3.74×10^7 Pa, 3.43×10^7 Pa and 3.52×10^7 Pa, respectively. Apparently, for the gyroid structure, it took the longest time to reach the maximum contact force and the peak von Mises stress for the gyroid structure was also the smallest, which proved that the gyroid structure had the best damping properties and energy dissipation. The G2 sample showed a comparably low density of 0.41 g cm^{-3} with the highest specific shielding effectiveness of 94.23 dB cm^3 g^{-1} (Fig. 5f), as well as excellent flexibility (Fig. 5g).

Conclusions

This study presents a scalable and versatile strategy for fabricating functional materials through multiscale synergistic customization, spanning from the macro- to nanoscale. The resultant hierarchical EMI shielding structures feature low density, high mechanical strength, and enhanced shielding effectiveness. PUA was employed to construct a range of TPMS architectures including gyroid, diamond, and I-WP geometries *via* the DLP technique. Copper nanocubes were subsequently conformally deposited onto the surface by chemical deposition, yielding a multiscale hierarchical design. The nanostructured surface significantly enhanced the electrical conductivity and enlarged the interfacial surface area, delivering consistent shielding performance across the X band. Among the geometries, gyroid-structured Cu/PUA exhibited the highest performance, with an average total shielding effectiveness of 38.29 dB at 2 mm thickness. Increasing thickness further enhanced absorption efficiency due to the continuous curvature and interconnected pore network that promotes multi-reflection pathways, achieving a shielding effectiveness of 76.64 dB, corresponding to the blocking of 99.999998% of incident waves. The highly porous structure afforded an ultralow density of 0.41 g cm^{-3}. Meanwhile, the compressive and flexural strengths reached 0.54 and 0.51 MPa, respectively, owing to the robust mechanical properties of the PUA substrates. This multiscale functionalization approach is readily adaptable to various geometries and materials, demonstrating broad scalability for EMI shielding systems.

Experimental

Materials

The polyurethane acrylate resin (PUA) used for 3D printing was provided by Chengdu Sicheng Advanced Material Co., Ltd, China. The density of the photo-cured solid polymer was 1.26 g cm^{-3}. Dopamine hydrochloride (DA·HCl, 98%), ammonia solution ($NH_3 \cdot H_2O$, 20 wt% in H_2O), copper(II) sulfate pentahydrate ($CuSO_4 \cdot 5H_2O$, 98%), ethylenediaminetetraacetic acid disodium salt dihydrate, (EDTA·2Na, 99%), 2,2′-bipyridyl(bpy, 99%), potassium hexacyanoferrate(II) trihydrate ($K4Fe(CN)_6 \cdot 3H_2O$, 98.5%), sodium hydroxide (NaOH, 97%), and formaldehyde solution (HCHO, 37 wt% in H_2O) were obtained from Sigma Aldrich, and silver nitrate ($AgNO_3$, 99.8%) was provided by Sinopharm Chemical Reagent Co., Ltd. Tris(hydroxymethyl)aminomethane (Tris, 99.9%) was purchased from Vivantis Technologies Sdn Bhd. The tape used for the tape test was Elcometer 99.

Preparation of the 3D-printed polymer lattice substrates

Three types of triply periodic minimal surface lattice structures (Diamond, Gyroid, and I-wrap) with a 2 mm unit cell size and 27% solid content were designed with MSLattice software and the cell structure is shown in Fig. 2a. The network type is a solid network. A DLP printer (Asiga MAX UV385) equipped with a 385 nm UV light source was employed to construct the 3D-printed polymer lattice substrates (PLS) with polyurethane acrylate resin.

The light intensity was set as 12 mW cm^{-2} and the layer thickness was 50 μm. The exposure times for the first layer and subsequent layers were 3s and 1s, respectively. The specific TPMS cells are shown in Fig. 1c. All the substrates were washed twice with ethanol and dried at 60 °C in a drying oven for 2 h before being collected for further use.

Cu coating of polymer lattice substrates

For Cu coating, we adopted an optimized method described in the article of Chang *et al.*[42] Specifically, the Cu coating process included two procedures: surface modification and chemical deposition of Cu.

For the surface modification process, the PLSs were soaked in the mixed solution (solvent: ethanol) of dopamine hydrochloride (1.5 g L^{-1}) and Tris (1.5 g L^{-1}) and stirred for 24 h for dopamine hydrochloride coating. The samples were then put on a laboratory bench for air drying. After being dried at room temperature for 2 h, the samples were immersed in silver ammonia solution (10 g L^{-1} $AgNO_3$ and 2 wt% ammonia solution) for 30 min to activate the surface.

For the chemical deposition process, the samples after surface modification were bathed in the mixed solution of $CuSO_4 \cdot 5H_2O$ (14 g L^{-1}), EDTA·2Na (12 g L^{-1}), $C_4O_6H_4KNa$ (20 g L^{-1}), 2,2′-bipyridyl (20 mg L^{-1}), $K_4Fe(CN)_6 \cdot 3H_2O$ (10 mg L^{-1}), NaOH (12 g L^{-1}), and HCHO (18 mL L^{-1}). The whole reaction system was placed in a water bath of 35 °C and magnetically stirred for 2 h for copper coating. The samples after Cu-coating were washed twice with deionized water and dried in a drying oven at 60 °C for 2 h. Finally, the Cu-coated PLSs (Cu/PLSs) were collected and appropriately stored for the subsequent electromagnetic interference (EMI) shielding test and characterization.

The adhesion of the Cu coating layer was evaluated according to ASTM D3359-23.

Electromagnetic interference (EMI) shielding test

The EMI shielding performance in a frequency range of 8.2–12.4 GHz of all the samples was tested using an Agilent N5232A Vector Network Analyzer. Samples were printed into a 22.86 × 10.16 mm^2 rectangular shape to precisely fit the waveguide fixture. The name and features of the tested samples are summarized in Table 2.

The reflection shielding effectiveness (SE_R), absorption shielding effectiveness (SE_A) and total shielding effectiveness (SE_T) were calculated by S_{11} and S_{21} parameters according to eqn (1)–(7):[43,44]

$$R = |S_{11}|^2 \tag{1}$$

$$T = |S_{21}|^2 \tag{2}$$

$$A = 1 - R - T \tag{3}$$

$$\mathrm{SE_R} = -10\log(1 - R) \tag{4}$$

$$\mathrm{SE_T} = -10\log(T) \tag{5}$$

$$\mathrm{SE_A} = -10\log\left(1 - \frac{A}{1 - R}\right) \tag{6}$$

$$\mathrm{SE_T} = \mathrm{SE_A} + \mathrm{SE_R} \tag{7}$$

Table 2 Samples for the EMI shielding test

Series	Sample name	Features	Thickness (mm)
C-series	C2, C4, C6	Bulk material without Cu coating	2, 4, 6
B-series	B2, B4, B6	Bulk material with Cu coating	2, 4, 6
—	D2	Diamond-structured material with Cu coating	2
—	DL2	Diamond-structured material without Cu coating	2
G-series	G2, G4, G6	Gyroid-structured material with Cu coating	2, 4, 6
GL-series	GL2, GL4, GL6	Gyroid-structured material without Cu coating	2, 4, 6
—	I2	I-wrap-structured material with Cu coating	2
—	IL2	I-wrap-structured material without Cu coating	2

Structural characterization

X-ray diffraction (XRD) spectra were recorded on a Rigaku Ultima IV diffractometer with Cu Kα radiation under the operation conditions of 30 kV and 20 mA. The scan range was 20–90° and the scan rate was 5° min^{-1}. The surface chemical compositions were investigated by X-ray photoelectron spectroscopy (XPS, Shimadzu Kratos AXIS SUPRA+) with Al-Kα irradiation, referencing the C 1s peaks at 284.8 eV for binding energy. Sample morphology was imaged using a scanning electron microscope (SEM, ZEISS GeminiSEM 360) equipped with an EDS system.

Mechanical and electrical property tests

A compression test and a three-point bending test were conducted to assess the mechanical properties of diamond, gyroid and I-wrap structures.

The compressive performance of the samples was evaluated using an electronic universal testing machine (Shimadzu AG25TB) at a loading rate of 0.5 mm min^{-1}. The PLSs were printed with a size of 10 × 10 × 10 mm for the compressive performance test. Besides, a cyclic compression test was conducted at the same loading rate to 1.5% compressive strain for 20 cycles.

The three-point bending test was conducted with an INSTRON 5500 universal testing machine at a loading rate of 8.53 mm min^{-1}. The PLSs were printed with a size of 50 × 12.7 × 2 mm for the compressive performance test. Besides, the cyclic three point bending test was conducted at the same loading rate to 1% flexural strain for 20 cycles.

For the compressive test, the compressive strength was defined by eqn (8):

$$\sigma_c = F_{\max}/S \tag{8}$$

where σ_c (MPa) is the compressive strength, $F_{\max}$ (N) is the compressive force at 10% deformation, and S (m^2) is the area of the sample.

For the three point bending test, the flexural strength was calculated by eqn (9):

$$\sigma_f = 3P_{\max}L/2bd^2 \tag{9}$$

where σ_f (MPa) is the flexural strength, $P_{\max}$ (N) is the load at the bending point, L (m) is the support span, b (m) is the width of the tested sample, and d (m) is the depth of the tested sample.

Material conductivity was evaluated using the KeithLink four-point conductivity probe measurement system. The conductivity of the uncoated PUA bulk material and Cu-coated bulk material was tested, with a sample size of 10 × 5 × 2 mm. The conductivity of the material was calculated by eqn (10):

$$\sigma = \frac{1}{\rho} = 1/(R_S \times T_f) \tag{10}$$

where σ (S m^{-1}) is the material conductivity, ρ (Ω m) is the material resistivity, R_S (Ω) is the sample resistance, and T_f (m) is the sample thickness.

Simulation

COMSOL simulation was conducted to evaluate the impact resistance of diamond, gyroid and I-wrap structures. The model is displayed in Fig. 5d. The original TPMS structures (10 × 10 × 2 mm) were designed using MS lattice software and imported into Comsol. The model is composed of a sphere at the top and a PLS at the bottom. The materials of the sphere and PLS were defined as stainless steel and PUA, respectively. The sphere was given an initial velocity of −1 m s^{-1} along the Z axis to simulate the impact process. The contact method was set as a penalty and a time span of 0.001 s was studied with a time step of 0.0001 s. The model only considered elastic deformation of the material. The impact resistance of the structures was evaluated by the contact force curves and von Mises stress distribution across the whole structure at maximum contact force.

Author contributions

Conceptualization: Y. M. and S. Z.; methodology: Y. M., U. J., S. Z., Z. W., and J. D.; investigation: Y. M., U. J., S. Z. and Z. W.; writing – original draft: Y. M. and S. Z.; writing – review and editing: Y. M., S. Z., U. J., W. Y., Y. Y. and J. D.; funding acquisition: Y. Y. and J. D.; and supervision: W. Y., Y. Y., and J. D.

Conflicts of interest

There are no conflicts to declare.

Data availability

The data supporting this article have been included in the paper and the SI. See DOI: https://doi.org/10.1039/d5nr02300a.

Acknowledgements

This work was supported by the Singapore Ministry of Education Academic Research Fund Tier 1 Grant (grant number: A-8002141-00-00 and A-8000215-01-00).

References

1 X. Jia, Y. Li, B. Shen and W. Zheng, *Composites, Part B*, 2022, **233**, 109652.

2 J. Liu, M.-Y. Yu, Z.-Z. Yu and V. Nicolosi, *Mater. Today*, 2023, **66**, 245–272.

3 R. Verma, P. Thakur, A. Chauhan, R. Jasrotia and A. Thakur, *Carbon*, 2023, **208**, 170–190.

4 N. Maruthi, M. Faisal and N. Raghavendra, *Synth. Met.*, 2021, **272**, 116664.

5 J. Cheng, C. Li, Y. Xiong, H. Zhang, H. Raza, S. Ullah, J. Wu, G. Zheng, Q. Cao, D. Zhang, Q. Zheng and R. Che, *Nano-Micro Lett.*, 2022, **14**, 80.

6 L. Yuan, S. Ding and C. Wen, *Bioact. Mater.*, 2019, **4**, 56–70.

7 R. Su, P. Liu, J. Chen, W. Wang, X. Chen, R. He and Y. Li, *Adv. Funct. Mater.*, 2025, 2500970.

8 P. Hua, X. Pan, J. Liu, X. Chen, M. Li, Y. Guo, X. Li, P. Leng, G. Fan, M. Zheng, K. Yu, P. Ma, C. Zhang and X. Shen, *Chem. Eng. J.*, 2025, **514**, 163246.

9 Y. Bai, B. Zhang, G. Fei and Z. Ma, *Chem. Eng. J.*, 2023, **478**, 147382.

10 S. M. Naqvi, T. Hassan, A. Iqbal, S. Zaman, S. Cho, N. Hussain, X. Kong, Z. Khalid, Z. Hao and C. M. Koo, *Nanoscale*, 2025, **17**, 8563–8576.

11 J. Feng, J. Fu, X. Yao and Y. He, *Int. J. Extreme Manuf.*, 2022, **4**, 022001.

12 Z. Islam, T. Ahmed, M. Mayyas and M. Abouheaf, *Mater. Today Commun.*, 2024, **40**, 109606.

13 S. Zhou, Y. Zhao, K. Zhang, Y. Xun, X. Tao, W. Yan, W. Zhai and J. Ding, *Nat. Commun.*, 2024, **15**, 6481.

14 S. Zhou, L. Yao, T. Zhao, H. Mei, L. Cheng and L. Zhang, *Carbon*, 2022, **196**, 253–263.

15 S. Zhou, H. Mei, M. Lu and L. Cheng, *Composites, Part A*, 2020, **139**, 106100.

16 S. Zhou, L. Yao, H. Mei, M. Lu, L. Cheng and L. Zhang, *Composites, Part B*, 2022, **230**, 109536.

17 S. Zhou, Y. Zhao, Y. Xun, Z. Wei, Y. Yang, W. Yan and J. Ding, *Chem. Rev.*, 2024, **124**, 3608–3643.

18 S. Zhou, H. Mei, P. Chang, M. Lu and L. Cheng, *Coord. Chem. Rev.*, 2020, **422**, 213486.

19 S. Zhou, L. Yao, H. Mei, K. G. Dassios, L. Cheng and L. Zhang, *Chem. Mater.*, 2022, **34**, 7167–7180.

20 S. Zhou, L. Yao, T. Zhao, H. Mei, K. G. Dassios, L. Cheng and L. Zhang, *Carbon*, 2023, **201**, 100–109.

21 H. Yan, X.-T. Qin, Y. Yin, Y.-F. Teng, Z. Jin and C.-J. Jia, *Appl. Catal., B*, 2018, **226**, 182–193.

22 X. Jiang, N. Koizumi, X. Guo and C. Song, *Appl. Catal., B*, 2015, **170–171**, 173–185.

23 M. Lykaki, E. Pachatouridou, S. A. C. Carabineiro, E. Iliopoulou, C. Andriopoulou, N. Kallithrakas-Kontos, S. Boghosian and M. Konsolakis, *Appl. Catal., B*, 2018, **230**, 18–28.

24 P. Gholami, L. Dinpazhoh, A. Khataee, A. Hassani and A. Bhatnagar, *J. Hazard. Mater.*, 2020, **381**, 120742.

25 C. Wang, Y. Wang, F. Zou, B. Fang, J. Zhao, H. Zhang, J. Guo, L. Jia and D. Yan, *Composites, Part B*, 2025, **291**, 112043.

26 C. Sun, D. Li, T. Liu, Q. An, C. Zhang, Y. Li and W. Liao, *Composites, Part B*, 2024, **280**, 111484.

27 Q. An, D. Li, W. Liao, T. Liu, D. Joralmon, X. Li and J. Zhao, *Adv. Mater.*, 2023, **35**, 2300659.

28 L. Ma, M. Hamidinejad, B. Zhao, C. Liang and C. B. Park, *Nano-Micro Lett.*, 2022, **14**, 19.

29 S. H. Lee, S. Yu, F. Shahzad, J. Hong, S. J. Noh, W. N. Kim, S. M. Hong and C. M. Koo, *Compos. Sci. Technol.*, 2019, **182**, 107778.

30 H. Xu, X. Yin, X. Li, M. Li, S. Liang, L. Zhang and L. Cheng, *ACS Appl. Mater. Interfaces*, 2019, **11**, 10198–10207.

31 L. Wang, L. Chen, P. Song, C. Liang, Y. Lu, H. Qiu, Y. Zhang, J. Kong and J. Gu, *Composites, Part B*, 2019, **171**, 111–118.

32 Z. Yu, T. Dai, S. Yuan, H. Zou and P. Liu, *ACS Appl. Mater. Interfaces*, 2020, **12**, 30990–31001.

33 H. Mei, X. Zhao, J. Xia, F. Wei, D. Han, S. Xiao and L. Cheng, *Mater. Des.*, 2018, **144**, 323–330.

34 M. Han, X. Yin, H. Wu, Z. Hou, C. Song, X. Li, L. Zhang and L. Cheng, *ACS Appl. Mater. Interfaces*, 2016, **8**, 21011–21019.

35 L. Yao, W. Cao, J. Zhao, Q. Zheng, Y. Wang, S. Jiang, Q. Pan, J. Song, Y. Zhu and M. Cao, *J. Mater. Sci. Technol.*, 2022, **127**, 48–60.

36 D. Huang, Y. Chen, L. Zhang and X. Sheng, *J. Mater. Sci. Technol.*, 2023, **165**, 27–38.

37 S. J. Mostafavi Yazdi, A. Lisitski, S. Pack, H. R. Hiziroglu and J. Baqersad, *Polymers*, 2023, **15**, 1911.

38 J. Song, K. Xu, J. He, H. Ye and L. Xu, *Polym. Compos.*, 2023, **44**, 2836–2845.

39 B. Fu, P. Ren, Z. Guo, Y. Du, Y. Jin, Z. Sun, Z. Dai and F. Ren, *Composites, Part B*, 2021, **215**, 108813.

40 Y. A. Bai, X. Wei, D. Dun, S. Bai, H. Zhou, B. Wen, X. Wang and J. Hu, *Polym. Compos.*, 2023, **44**, 1951–1966.

41 S.-Q. Zhu, J.-C. Shu and M.-S. Cao, *Nanoscale*, 2022, **14**, 7322–7331.

42 P. Chang, H. Mei, Y. Zhao, W. Huang, S. Zhou and L. Cheng, *Adv. Funct. Mater.*, 2019, **29**, 1903588.

43 R. Ravindren, S. Mondal, P. Bhawal, S. M. N. Ali and N. C. Das, *Polym. Compos.*, 2019, **40**, 1404–1418.

44 B. Shen, Y. Li, W. Zhai and W. Zheng, *ACS Appl. Mater. Interfaces*, 2016, **8**, 8050–8057.